

Lattice distortion leads to glassy thermal transport in crystalline $\text{Cs}_3\text{Bi}_2\text{I}_6\text{Cl}_3$

Zezhu Zeng,^{1,*} Zheyong Fan,² Chen Chen,^{3,†} Ting Liang,⁴ Yue Chen,⁵ Geoff Thornton,⁶ and Bingqing Cheng^{7,1,‡}

¹*The Institute of Science and Technology Austria, Am Campus 1, 3400 Klosterneuburg, Austria*

²*College of Physical Science and Technology, Bohai University, Jinzhou 121013, China*

³*School of Physical Sciences, Great Bay University, Dongguan, Guangdong, China*

⁴*Department of Electronic Engineering and Materials Science and Technology Research Center, The Chinese University of Hong Kong*

⁵*Department of Mechanical Engineering, The University of Hong Kong, Pokfulam Road, Hong Kong SAR, China*

⁶*London Centre for Nanotechnology, University College London, London WC1H 0AJ, United Kingdom*

⁷*Department of Chemistry, University of California, Berkeley, CA, USA*

(Dated: July 29, 2024)

The glassy thermal conductivities observed in crystalline inorganic perovskites such as $\text{Cs}_3\text{Bi}_2\text{I}_6\text{Cl}_3$ is perplexing and lacking theoretical explanations. Here, we first experimentally measure such its thermal transport behavior from 20 K to 300 K, after synthesizing $\text{Cs}_3\text{Bi}_2\text{I}_6\text{Cl}_3$ single crystals. Using path-integral molecular dynamics simulations driven by machine learning potentials, we reveal that $\text{Cs}_3\text{Bi}_2\text{I}_6\text{Cl}_3$ has large lattice distortions at low temperatures, which may be related to the large atomic size mismatch. Employing the regularized Wigner thermal transport theory, we reproduce the experimental thermal conductivities based on lattice-distorted structures. This study thus provides a framework for predicting and understanding glassy thermal transport in materials with strong lattice disorder.

A foundational theory for the lattice thermal conductivity (κ) in crystals was proposed by Peierls in 1929 [1] based on the phonon gas picture: κ has a T^3 behavior at low temperatures, followed by a decrease with a T^{-1} dependence due to Umklapp phonon scattering. This behavior is observed in many materials, such as thermoelectric AgTlI_2 [2] and inorganic perovskite CsPbI_3 [3], as illustrated in Fig. 1.

For glasses, such as amorphous Si [4] and SiO_2 [5], the behavior of κ is distinct (see Fig. 1): At low temperatures ($T \lesssim 1$ K), $\kappa(T) \sim T^2$, which may be explained by quantum tunneling [6]; between 5 K and 25 K, $\kappa(T)$ plateaus, which may be related to the boson peak of glasses [7]; At higher T , κ increases with temperature, which can be explained by the Allen-Feldman (AF) model [8, 9] based on decoupled harmonic oscillators.

However, κ of some crystalline materials do not follow the typical behavior of crystals but are rather glassy, e.g. layered perovskite $\text{Cs}_3\text{Bi}_2\text{I}_6\text{Cl}_3$ [10], quasi-one-dimensional perovskite BaTiS_3 [11, 12], and Ruddlesden-Popper perovskites $\text{Ba}_3\text{Zr}_2\text{S}_7$ and $\text{Ba}_4\text{Zr}_2\text{S}_{10}$ [13]. In this study, we synthesized a high-quality single crystal (see Methods section for details) of $\text{Cs}_3\text{Bi}_2\text{I}_6\text{Cl}_3$ (space group $P\bar{3}m1$) and measured its κ from 20 K to 300 K (see Fig. 1). Interestingly, both κ_x and κ_z in $\text{Cs}_3\text{Bi}_2\text{I}_6\text{Cl}_3$ deviate from the expected T^3 dependence at low T and lack crystalline-like peak in the entire temperature range. In addition, κ_x exhibits an unusual wide plateau region (60–150 K), while κ_z steadily increases with increasing temperature.

Some other materials also exhibit measured glassy κ below room temperature. For example, $(\text{KBr})_{1-x}(\text{KCN})_x$ [14, 15] transitions from crystalline to glassy κ with an increase in the molar fraction of KCN, which was attributed to binary doping. The glassy κ in clathrates $\text{Sr}_8\text{Ga}_{16}\text{Ge}_{30}$ and $\text{Eu}_8\text{Ga}_{16}\text{Ge}_{30}$

[16] was rationalized by the rattling atoms within cage-like structures. In contrast, $\text{Cs}_3\text{Bi}_2\text{I}_6\text{Cl}_3$ lacks the binary doping as mixed crystals or a cage-like structure, suggesting a distinct mechanism behind its glassy κ . Acharyya *et al.* [10] first reported the glassy κ of crystalline $\text{Cs}_3\text{Bi}_2\text{I}_6\text{Cl}_3$, and rationalized the slow increase of κ near room temperature based on local atomic disorder and low sound velocity, but the mechanism governing the glassy κ at lower temperatures remains unclear.

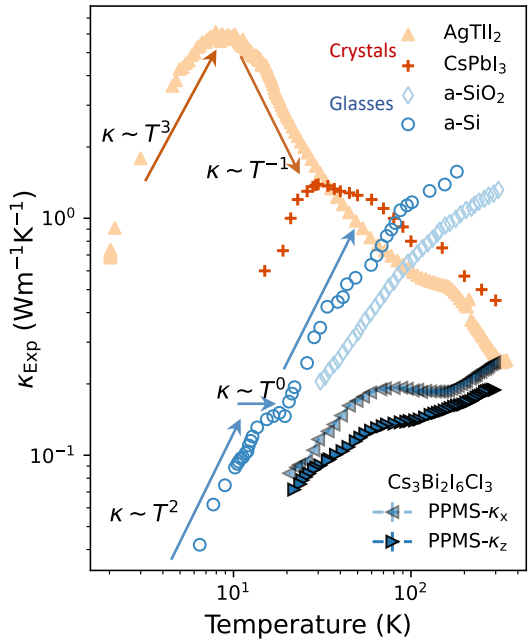


FIG. 1. Experimental lattice thermal conductivity (κ) for AgTlI_2 [2] and CsPbI_3 [3] crystals, amorphous Si [4] and SiO_2 [5] glasses, and single crystal $\text{Cs}_3\text{Bi}_2\text{I}_6\text{Cl}_3$ measured by us for both parallel (κ_z) and perpendicular ($\kappa_x = \kappa_y$) directions relative to the Bridgman growth direction.

* zzeng@ist.ac.at

† ccmldn@gbu.edu.cn

‡ bingqingcheng@berkeley.edu

It is challenging to calculate κ for solids with strong anharmonicity at low temperatures: Regular molecular dynamics (MD) does not consider nuclear quantum effects (NQE), while quantum MD methods, such as path integral MD (PIMD) [17, 18], centroid MD (CMD) [19], ring polymer MD (RPMD) [20], and thermostatted ring polymer MD (TRPMD) [21], can incorporate NQE but need to make approximations on the nonlinear heat flux operator [22, 23]. On the other hand, recent advancements [24] in lattice dynamics such as Wigner transport equation (WTE) [24–26] and quasi harmonic Green-Kubo (QHGK) theory [27, 28] offer new methods to compute κ of complex materials with strong anharmonicity by considering both propagative (κ_{pg}) and diffusive (κ_{diff}) thermal conductivities. However, a previous study [29] reported the divergence of κ_{pg} at low T when computing κ of vitreous silica using WTE, due to the finite-size effects. Although WTE can further simplify to the AF model via considering all harmonic modes with infinitesimal linewidth at the center of Brillouin zone to compute κ of glasses and thus avoid divergence, the AF model neglects anharmonic atomic vibrations [8, 30]. Very recently, regularized WTE (rWTE) [29] was proposed to overcome the divergence and thus can compute the κ of glasses accounting for both anharmonicity and quantum Bose-Einstein statistics of atomic vibrations.

Lattice distortion at low temperatures

We first constructed a machine-learning-based neuroevolution potential (NEP) [32, 33], for $\text{Cs}_3\text{Bi}_2\text{I}_6\text{Cl}_3$ across a broad range of temperature and strain, based on the PBEsol functional [34] with the D3 dispersion correction [35]. We then simulated the crystal structure of $\text{Cs}_3\text{Bi}_2\text{I}_6\text{Cl}_3$ between 25 K and 300 K, using PIMD simulations driven by the NEP. Fig. 2a shows the projection of atom positions onto the two-dimensional a - b plane in the unit cell. At 250 K, all atoms vibrate near their equilibrium lattice positions in the $P\bar{3}m1$ crystal structure, consistent with results of the crystal structure characterization from our single-crystal XRD experiment at 300 K (Table S2 of Supplementary Information). In contrast, at 25 K the atomic position distributions have multiple peaks. At 100 K, the peaks grow in size but become closer together, suggesting a reduction in lattice distortion but with stronger thermal vibrations. Note that the scattered spots at 25 K and 100 K still cluster around the $P\bar{3}m1$ lattice sites, thus the calculated radial distribution functions in Fig. 2b show characteristic peaks associated with crystals across the whole temperature range.

To further quantify the lattice distortion, we computed the mean square displacement (MSD) of the four elements using the $P\bar{3}m1$ structure as a reference. As shown in Fig. 2c, MSD decreases with increasing temperature, with a notable drop between 200 K and 250 K that corresponds to the structure transition from disorder to order. Above 250 K, as the crystal structure reverts to the $P\bar{3}m1$ phase, MSD values increase with temperature, which is a typical tendency in ordered crystals.

The strong disorder in crystalline $\text{Cs}_3\text{Bi}_2\text{I}_6\text{Cl}_3$ at low temperatures is unusual for two reasons: First, in many disor-

dered crystals, only a part of elements exhibit correlated disorder [36–38], where lattice distortions follow a specific pattern with spatial correlations, e.g. in thermoelectric PbTe the Pb atoms exhibit large deviation along specific $\langle 100 \rangle$ directions [39], in metal-organic frameworks [40] the correlated distribution of linker vacancies leads to a patterned disordering. In contrast, all elements in $\text{Cs}_3\text{Bi}_2\text{I}_6\text{Cl}_3$ have uncorrelated disorder. Second, the other disordered crystals are typically ordered at low T and become disordered at high T [36], while $\text{Cs}_3\text{Bi}_2\text{I}_6\text{Cl}_3$ is opposite.

Strong lattice distortion can lead to substantial phonon-disorder scatterings. To investigate this, we used a $16 \times 16 \times 16$ supercell with 57344 atoms to compute the longitudinal and transverse current correlation functions based on RPMD trajectories at 25 K and 250 K (as shown in Fig. 2d with heatmaps), which incorporates both full-order lattice anharmonicity and NQE. The longitudinal and transverse current correlation functions [41], $C_L(\mathbf{q}, t)$ and $C_T(\mathbf{q}, t)$ are

$$C_L(\mathbf{q}, t) = \frac{1}{N} \langle \mathbf{j}_L(\mathbf{q}, t) \cdot \mathbf{j}_L(-\mathbf{q}, 0) \rangle, \quad (1)$$

$$C_T(\mathbf{q}, t) = \frac{1}{N} \langle \mathbf{j}_T(\mathbf{q}, t) \cdot \mathbf{j}_T(-\mathbf{q}, 0) \rangle,$$

where $\mathbf{j}_L(\mathbf{q}, t)$ and $\mathbf{j}_T(\mathbf{q}, t)$ are given by

$$\mathbf{j}_L(\mathbf{q}, t) = \sum_i^N (\mathbf{v}_i(t) \cdot \hat{\mathbf{q}}) \hat{\mathbf{q}} e^{i\mathbf{q} \cdot \mathbf{r}_i(t)}, \quad (2)$$

$$\mathbf{j}_T(\mathbf{q}, t) = \sum_i^N [\mathbf{v}_i(t) - (\mathbf{v}_i(t) \cdot \hat{\mathbf{q}}) \hat{\mathbf{q}}] e^{i\mathbf{q} \cdot \mathbf{r}_i(t)},$$

with N , \mathbf{q} , \mathbf{r}_i , and \mathbf{v}_i representing the total number of atoms, wave vector, atomic position vector, and velocity vector, respectively. For comparison, Fig. 2d also shows the renormalized phonon dispersions at 25 K and 250 K using gray lines, calculated using the temperature-dependent effective potential (TDEP) [42] based on the $P\bar{3}m1$ structure. TDEP incorporates temperature-dependent phonon frequency correction arising from lattice anharmonicity beyond the third order. At 250 K, the phonon modes are well-defined and all real, with frequencies from current correlation functions closely matching those derived from TDEP calculations, which reveals that higher-than-third-order anharmonic renormalization to harmonic phonon frequencies (see Fig. S12) at 0 K. In contrast, phonon scattering at 25 K is significantly more severe than at 250 K, especially along the wave vector paths from Γ to A and from M to Γ in the first Brillouin zone, indicating substantial phonon-disorder interactions. Additionally, we observe unusual overdamped modes near the Brillouin zone center at 25 K, as previously noted in perovskite CsPbBr_3 [43], while no imaginary modes are observed in TDEP results. This comparison suggests that lattice dynamics with low-order perturbation is not suitable for comprehending vibrational modes and heat transport of strongly disordered $\text{Cs}_3\text{Bi}_2\text{I}_6\text{Cl}_3$ at low temperatures.

To rationalize the large lattice distortion, we computed potential energy surfaces (PES) of the imaginary phonon modes at high-symmetry points by displacing corresponding atoms

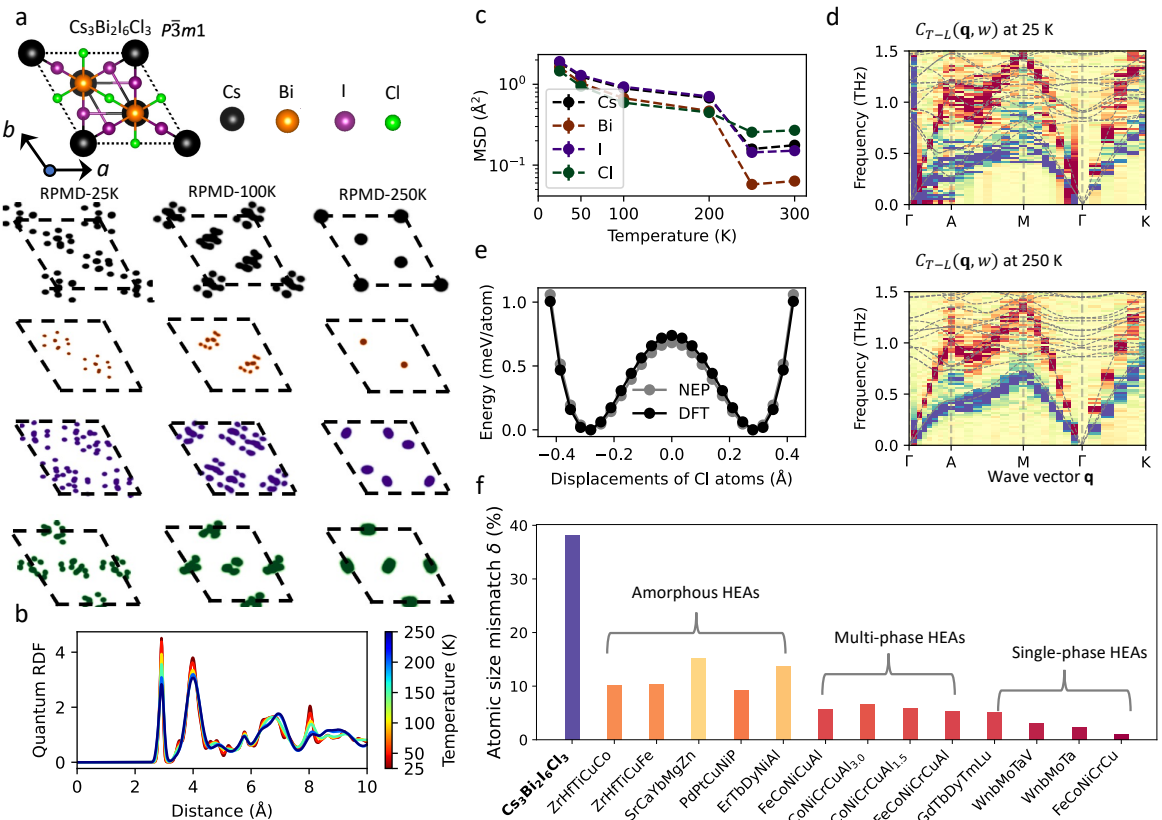


FIG. 2. **a** Atomic probability distribution of four elements in $\text{Cs}_3\text{Bi}_2\text{I}_6\text{Cl}_3$ from NEP ring-polymer molecular dynamics (RPMD) simulations at 25 K, 100 K, and 250 K. **b** Calculated radial distribution function (RDF) of $\text{Cs}_3\text{Bi}_2\text{I}_6\text{Cl}_3$ at different temperatures based on the RPMD simulations. **c** Mean square displacements (MSD) from 25 K to 300 K. **d** Transverse (red) and longitudinal (blue) current correlation functions $C_{T-L}(\mathbf{q}, \omega)$ as a function of wave vector \mathbf{q} and frequency ω , calculated from RPMD trajectories at 25 K and 250 K. The dashed curves show phonon dispersions of $\text{Cs}_3\text{Bi}_2\text{I}_6\text{Cl}_3$, computed using the temperature-dependent effective potential (TDEP) approach with the $P\bar{3}m1$ crystal structure. **e** Potential energy surfaces of the soft mode at Γ point calculated using NEP and DFT by displacing Cl atoms in the unit cell. **f** Atomic size mismatch parameter (δ) for crystalline $\text{Cs}_3\text{Bi}_2\text{I}_6\text{Cl}_3$ and selected high-entropy alloys (HEAs) [31] with single-phase, multiple-phase, and amorphous-phase structures.

along their eigenvectors. We found shallow and double-well PES shown in Fig. 2e (for Γ point) and Fig. S12 (for other high-symmetry points), leading to significant atomic displacements towards two local minima with large distances of about 0.7 Å. In Fig. 2e, the energy barrier along the imaginary mode of Γ point is only 0.7 meV/atom, which is about energy associated with thermal fluctuation at about 10 K. At temperatures below or similar to this, the atoms tends to stay in the local minima, and at high temperatures the atoms can overcome the energy barrier and vibrate around the lattice positions. This may explain the multiple peaks at 25 K in Fig. 2a, with cluster into a single peak upon heating to 250 K.

Lattice distortions in crystals are often attributed to atomic size mismatch [44], i.e.

$$\delta\% = 100\% \sqrt{\sum_{i=1}^n c_i \left(1 - \frac{r_i}{\sum_{j=1}^n c_j r_j}\right)^2}, \quad (3)$$

where c_i and r_i denote the atomic fraction and atomic radius

of the i th element, respectively. High-entropy alloys (HEAs) with large δ often have strong lattice distortions [45]. In comparison, the δ of $\text{Cs}_3\text{Bi}_2\text{I}_6\text{Cl}_3$ is larger than that of typical HEAs, as shown in Fig. 2f. The δ mainly come from the large difference in atomic radii of Cs and Cl. The large δ not only shed light on the large lattice distortions, but also help explain why the κ of $\text{Cs}_3\text{Bi}_2\text{I}_9$ exhibits typical crystalline behavior [46] while the κ of $\text{Cs}_3\text{Bi}_2\text{I}_6\text{Cl}_3$ is glassy.

Thermal conductivity follows a glass-like mechanism

We computed the κ of $\text{Cs}_3\text{Bi}_2\text{I}_6\text{Cl}_3$ using both molecular dynamics and lattice dynamics. Classical MD simulations with Green-Kubo (GK) theory offer a straightforward method to compute the κ of disordered crystals, as atomic disorder is inherently included. At T above 150 K, the computed κ (see Fig. S9) agree well with our experimental data. However, below 150 K, the calculations show an distinct overestimation, due

to the lack of NQE in classical MD. To include NQE, we also performed TRPMD simulations with GK theory. The κ calculated from TRPMD (see Fig. S9) does not show considerable differences from those computed using classical MD (i.e., still overestimating the experimental κ at T below 150 K), indicating potential limitations of the GK method within TRPMD for accurately assessing κ at low T . This limitation arises from the ambiguous definition of the non-linear heat flux operator in PIMD-based simulations [22, 23].

Classical homogeneous non-equilibrium MD (HNEMD) simulations [47, 48], with an empirical quantum correction [49] (detailed in Methods), provide an alternative way to assess κ without defining the heat flux in the PIMD-based framework. The κ from HNEMD are shown in Fig. 3. Classical HNEMD κ show an overestimation along both the x and z directions at T below 150 K compared to the measurements, similar to the observation from the GK results with classical MD. After applying the harmonic quantum correction [49] accounting for the modal heat capacity, the corrected κ_z agrees well with the experimental data. However, κ_x remains overestimated and fails to reproduce the glassy behavior. This could be due to the limited scope of the harmonic quantum correction, which considers only the quantum effects on the heat capacity, but does not address mode-mode occupations that can affect phonon coupling.

As the MD based methods are not able to reproduce the experimental glassy κ of $\text{Cs}_3\text{Bi}_2\text{I}_6\text{Cl}_3$, we resorted to lattice dynamics, which can incorporate the NQE. We first employed the WTE [25, 29]:

$$\kappa = \frac{1}{\mathcal{V}N_c} \sum_{\mathbf{q}, s, s'} \frac{\omega(\mathbf{q})_s + \omega(\mathbf{q})_{s'}}{4} \left(\frac{C(\mathbf{q})_s}{\omega(\mathbf{q})_s} + \frac{C(\mathbf{q})_{s'}}{\omega(\mathbf{q})_{s'}} \right) \frac{\|\mathbf{v}(\mathbf{q})_{s, s'}\|^2}{3} \times \pi \mathcal{F}_{[\Gamma(\mathbf{q})_s + \Gamma(\mathbf{q})_{s'}]} (\omega(\mathbf{q})_s - \omega(\mathbf{q})_{s'}), \quad (4)$$

where \mathcal{V} is the volume of the unit cell, N_c is the number of \mathbf{q} -points in the summation, s and s' are band indices at the wave vector \mathbf{q} (with κ_{pg} derived when $s = s'$ and κ_{diff} derived when $s \neq s'$), ω is the vibrational frequency, $C(\mathbf{q})_s$ is the specific heat, and $\mathbf{v}(\mathbf{q})_{s, s'}$ is the velocity operator. Γ is the anharmonic linewidth, and the Lorentzian distribution \mathcal{F} , having a full width at half maximum (FWHM) equal to $\Gamma(\mathbf{q})_s + \Gamma(\mathbf{q})_{s'}$, is defined as:

$$\mathcal{F}_{[\Gamma(\mathbf{q})_s + \Gamma(\mathbf{q})_{s'}]} (\omega(\mathbf{q})_s - \omega(\mathbf{q})_{s'}) = \frac{1}{\pi} \frac{\frac{1}{2} (\Gamma(\mathbf{q})_s + \Gamma(\mathbf{q})_{s'})}{(\omega(\mathbf{q})_s - \omega(\mathbf{q})_{s'})^2 + \frac{1}{4} (\Gamma(\mathbf{q})_s + \Gamma(\mathbf{q})_{s'})^2}. \quad (5)$$

At high T (250 K and 300 K), the structure of $\text{Cs}_3\text{Bi}_2\text{I}_6\text{Cl}_3$ is the $P\bar{3}m1$ crystal (see Fig. 2a). We used this structure in the WTE calculation, which accounts for thermal expansion, renormalized phonon frequencies using TDEP [42], and four-phonon interactions [50, 51], essential corrections to accurately treat perovskites with strong lattice anharmonicity [52, 53]. The calculated values of κ are consistent with the experimental observations as shown in Fig. 3. Further insights into thermal transport are obtained from the spectral- κ at 300 K, as shown in Fig. S10. Notably, κ_{pg} exhibits an

extremely low value of $\sim 0.18 \text{ W/mK}$ at 300 K along both x and z directions, and κ_{diff} along the z -axis is almost equal to κ_{pg} along the z -axis, implying considerable diffusive heat transport in $\text{Cs}_3\text{Bi}_2\text{I}_6\text{Cl}_3$ at room temperature.

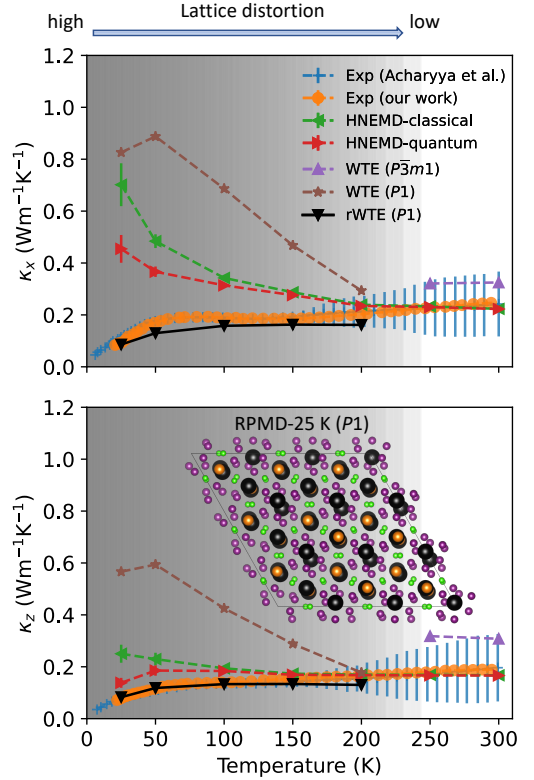


FIG. 3. Calculated κ for single crystal $\text{Cs}_3\text{Bi}_2\text{I}_6\text{Cl}_3$. Green and red triangles show results from homogeneous nonequilibrium MD (HNEMD) simulations, with and without empirical quantum corrections. At 250 K and 300 K, the purple triangles show the κ calculated using the Wigner Transport Equation (WTE) with $P\bar{3}m1$ structure. At T between 25 K and 200 K, the stars and inverted triangles show the WTE and regularized WTE κ on top of the relaxed distorted structures. A disordered structure at 25 K (252 atoms) is shown in the inset. Additionally, the circle and cross symbols show experimental κ from our measurements and from Ref. [10], respectively.

Note that WTE can only simplify to the AF model to compute κ of glasses [29], thus this simplification ignores the anharmonic atomic vibration in glasses. To address these limitations, Simoncelli *et al.* [29] proposed a regularization to WTE (rWTE) to compute the κ of glasses including the anharmonicity using a finite-size model with Fourier interpolation. This method introduces a two-parameter distribution for \mathcal{F} , denoted as $\mathcal{F}_{[\Gamma(\mathbf{q})_s + \Gamma(\mathbf{q})_{s'}, \eta]}$, which is derived by convolving a Lorentzian with a full width at half maximum of $\Gamma(\mathbf{q})_s + \Gamma(\mathbf{q})_{s'}$ and a Gaussian with a variance of $\eta^2\pi/2$. The convolution is often referred to as the Voigt function (see the Methods section for more details).

The order-to-disorder transition in $\text{Cs}_3\text{Bi}_2\text{I}_6\text{Cl}_3$ raises a question about the nature of its thermal transport below 200 K: Is the mechanism crystal-like or glass-like? If the former, κ can be calculated using WTE. If the latter, κ should follow the

thermal transport mechanism of amorphous solids outlined in the rWTE.

To answer this, we used both the WTE and rWTE to calculate the κ of $\text{Cs}_3\text{Bi}_2\text{I}_6\text{Cl}_3$ below 200 K (the rWTE calculation workflow is detailed in Fig. S4). In theory, an infinitely large supercell would be required to capture the global lattice disorder. In practice, we performed an approximation using a supercell with 252 atoms and $3 \times 3 \times 3$ \mathbf{q} -meshes coupled with Fourier interpolations [29], after a convergence test (see Fig. S7 of SI). This supercell was used to run PIMD simulations at temperatures from 25 K to 200 K. After equilibration, a snapshot was randomly taken from the PIMD trajectories and then relaxed using the NEP. The relaxed structure (shown in Fig. 3) has inherent lattice distortion, with its symmetry classified as $P1$. This $P1$ structure then served as the initial equilibrium configuration for computing both WTE and rWTE κ . Another challenge is that computing anharmonic linewidths with perturbation theory is extremely time-consuming for a unit cell with hundreds of atoms. We thus applied an analytical function (see the Methods section) to fit the linewidths as functions of frequency.

The WTE and rWTE κ are shown in Fig. 3. At temperatures below 200 K, the κ computed using WTE for the $P1$ structure is overestimated. In contrast, κ computed using rWTE for the $P1$ structure aligns closely with experimental results in both magnitude and temperature trends. The reason why rWTE is better suited to predict the κ of $\text{Cs}_3\text{Bi}_2\text{I}_6\text{Cl}_3$ at low T could be attributed to the significant atomic disorder in $\text{Cs}_3\text{Bi}_2\text{I}_6\text{Cl}_3$ at low temperatures, which disrupts the lattice definition. This disruption indicates that heat carriers are likely not phonons (collective lattice vibrations), further suggesting the material exhibits glassy heat transport characteristics.

Finally, we rule out two other possible factors that may affect the κ comparisons between calculations and measurements. To examine phonon-boundary scattering effects, we computed the spectral mean free path (MFP) of $\text{Cs}_3\text{Bi}_2\text{I}_6\text{Cl}_3$ at 25 K. At 25 K, the maximum MFP (Fig. S11) along the x direction is approximately 400 nm, which is significantly shorter than the dimensions of the single crystal sample ($2.5 \times 2.5 \times 6$ mm 3) used to measure κ . We also examined the phonon-isotope effects [54] by considering different isotope masses in HNEMD simulations, and find that these effects are negligible for κ . Therefore, neither grain size effects nor phonon-isotope scatterings can account for the overestimated WTE κ with the $P1$ structure below 200 K, further indicating the necessity of using rWTE to correctly comprehend glassy κ of $\text{Cs}_3\text{Bi}_2\text{I}_6\text{Cl}_3$ below 200 K.

CONCLUSION

In summary, we synthesized a single-crystal inorganic halide perovskite $\text{Cs}_3\text{Bi}_2\text{I}_6\text{Cl}_3$ and measure its glassy κ from 20 to 300 K. We developed a machine-learning neuroevolution potential and performed PIMD simulations to investigate its atomic structure. The atomic probability distribution from PIMD trajectories reveal an order-to-disorder transition at ~ 200 K, indicating significant uncorrelated lattice distortion

in $\text{Cs}_3\text{Bi}_2\text{I}_6\text{Cl}_3$. Given the disordered structure in $\text{Cs}_3\text{Bi}_2\text{I}_6\text{Cl}_3$ at low temperatures, we employed both lattice dynamics and molecular dynamics approaches to compute its κ . We concluded that regularized WTE is best suited to rationalize its glassy κ at low temperatures, suggesting that the heat transport mechanism of $\text{Cs}_3\text{Bi}_2\text{I}_6\text{Cl}_3$ is akin to that of amorphous materials. Our κ computation workflow considers both nuclear quantum effects and atomic disorder, providing a framework for comprehending and modeling heat transport in strongly disordered materials.

METHODS

Experiments

Sample preparation The raw materials CsCl (99.9%, Innochem) and BiI_3 (99.99%, Aladdin) were sealed in a quartz tube and placed in a two-zone vertical furnace. The tube was gradually heated to 1023 K, where it was maintained for 40 hours. Subsequently, the lower zone of the furnace was cooled to 903 K over an 8-hour period. The temperatures in both zones were then decreased at a rate of 3 K/h for a total of 90 hours. Finally, the heating was turned off to complete the cooling process, allowing the resulting $\text{Cs}_3\text{Bi}_2\text{I}_6\text{Cl}_3$ to crystallize.

Sample characterization Single-crystal X-ray diffraction (XRD) studies were performed on a Bruker D8 QUEST diffractometer equipped with a $\text{Mo K}\alpha$ radiation source ($\lambda = 0.71073$ Å) at room temperature. The crystal structure solution and refinements of $\text{Cs}_3\text{Bi}_2\text{I}_6\text{Cl}_3$ is carried out using single crystal XRD at room temperature, as shown in Table S2. The $\text{Cs}_3\text{Bi}_2\text{I}_6\text{Cl}_3$ sample possesses the trigonal structure with a space group $P\bar{3}m1$. As presented in Figure S1, all the peaks of powder XRD pattern fit well with the $\text{Cs}_3\text{Bi}_2\text{I}_6\text{Cl}_3$ pattern. The XRD pattern tested on the cleavage plane shows that the crystal is liable to fracture along the $(00l)$ crystal plane due to the weak chemical bonds between the layers.

Thermal conductivity measurement The cleavage plane of crystalline $\text{Cs}_3\text{Bi}_2\text{I}_6\text{Cl}_3$ is the $(00l)$ (l is an integer) plane. To measure the κ in the cleavage plane (κ_x or κ_y) and across the cleavage plane (κ_z), two cubes (sectional area: 2.5 mm \times 2.5 mm; height: 6 mm) were cut from the obtained crystal for the thermal conductivity measurement. The low-temperature κ was measured using a physical properties measurement system (PPMS, Quantum Design). The $\text{Cs}_3\text{Bi}_2\text{I}_6\text{Cl}_3$ crystal is nonconductive [10], so the measured thermal conductivity is equal to the lattice thermal conductivity. Our measurements of κ agree very well with the previous experiments [10].

Calculations

Constructing the MLP. We utilized the neural-network-based neuroevolution potential (NEP) approach [32, 33] to develop a MLP for $\text{Cs}_3\text{Bi}_2\text{I}_6\text{Cl}_3$. The procedure begins with obtaining the relaxed structure at 0 K using the VASP package [55, 56]. Subsequently, we conducted *ab initio* molecular dynamics (AIMD) simulations in the NVT ensemble with a 2×2

$\times 2$ supercell (112 atoms) at temperatures of 20 K, 50 K, 100 K, 200 K, 300 K, 400 K, 500 K, and 600 K, randomly selecting ~ 50 configurations for training at each temperature. Furthermore, AIMD simulations with the NPT ensemble, varying pressure (± 1 Gpa and 2.5 Gpa) at specific temperatures (25 K, 150 K and 300 K), were performed and ~ 30 configurations were randomly chosen for each condition to account for lattice thermal expansion. Taking into account the two-dimensional layered structure of $\text{Cs}_3\text{Bi}_2\text{I}_6\text{Cl}_3$, we further selected configurations using the initial NEP, conducting MD simulations with D3 dispersion correction [57] at 25 K, 100 K, 200 K, and 300 K. The final training set comprises 1000 configurations. We used the PBEsol functional [34] in the DFT calculations, known for its accuracy in predicting lattice constants and κ in strongly anharmonic crystals [58]. All AIMD simulations employ an energy cutoff value of 400 eV and a Γ -centered $1 \times 1 \times 1$ k -point mesh with the PBEsol [34] functional. We raised the energy cutoff to 550 eV with a denser $3 \times 3 \times 3$ k -point mesh to perform accurate single-point DFT calculations and obtain the energies and atomic forces of the selected configurations. We used the GPUMD package [33, 59] to train the NEP model, and the final training/test root mean square errors (RMSEs) for energy, atomic force, and virial are 0.35/0.33 meV/atom, 0.027/0.026 eV/Å, and 3.79/3.33 meV/atom, respectively.

Cross validation of the NEP model. To validate our NEP model, we performed path integral molecular dynamics (PIMD) simulations at selected temperatures (25 K, 100 K, 300 K, and 400 K), both with and without the D3 correction, and sampled a number of configurations for subsequent single-point DFT calculations. Parity plots between NEP and DFT for the energies and forces of the sampled configurations are presented in Figs. S2 and S3. Without the D3 correction, The RMSEs for energy and force are 0.36 meV/atom and 0.025 eV/Å, respectively, while they are 0.31 meV/atom and 0.021 eV/Å, respectively, with the D3 correction. The lattice constants (Table S1) and atomic potential energy surfaces of some soft modes (Fig. S12) from DFT and NEP calculations are in good agreement.

MD simulations We performed path-integral-based and classical MD simulations using the GPUMD package [33, 59], with a timestep of 1 fs. PIMD/RPMD simulations were conducted at 25 K and 50 K with 64 beads, at 100 K, 150 K, and 200 K with 32 beads, and at 250 K and 300 K with 16 beads. Convergence tests for the number of beads in these simulations are provided in Fig. S6. For quantum MD simulations, we started with PIMD simulations in an NPT ensemble to obtain equilibrium structures at the specified temperatures. Following this, we run 0.5 ns RPMD simulations to collect atomic trajectories to calculate atomic probability distributions and radial distribution functions, or TRPMD simulations to compute κ based on the Green-Kubo relationship. Further details on the computation of κ using Green-Kubo theory with TRPMD simulations are available in Fig. S9 and Note S1 of SI. For classical HNEMD simulations, we used an NPT ensemble, employing a stochastic cell rescaling barostat [60] in combination with the stochastic velocity rescaling thermostat [61] to calculate κ . We conducted a thorough examination of size effects and the selection of external forces during HNEMD

simulations.

Anharmonic linewidths and its analytical function Calculating vibrational linewidths rigorously in a complex, atom-heavy primitive cell is highly time-consuming. To address this challenge, previous studies [29, 62, 63] introduced a coarse-grained function, $\Gamma_a[\omega]$, in various formats to reduce computational demands. The only required input to obtain $\Gamma_a[\omega]$ is the exact linewidths at $\mathbf{q} = 0$. Simoncelli *et al.* [29] demonstrated that the use of the single-valued function $\Gamma_a[\omega]$ leads to practically identical results for the conductivity of rWTE compared to exact linewidths. This fitting was demonstrated to reliably capture the linewidths of $\nu\text{-SiO}_2$ [29], $\text{Mg}_2\text{Si}_{1-x}\text{Sn}_x$ [62], amorphous Si [64] and Al_2O_3 [63].

Here we used the RPMD simulations with normal mode decomposition method [65, 66] to obtain the exact anharmonic linewidths of all vibrational modes at $\mathbf{q} = 0$, and then we fit [29] the $\Gamma_a[\omega]$ as

$$\Gamma_a[\omega] = \frac{1}{\sqrt{\frac{1}{(\Gamma_1[\omega])^2} + \frac{1}{(\Gamma_2[\omega])^2}}}, \quad (6)$$

where $\Gamma_1[\omega]$ and $\Gamma_2[\omega]$ are defined as

$$\Gamma_1[\omega] = \frac{\sum_{\mathbf{q}=0,s} \frac{1}{\sqrt{2\pi\sigma^2}} \exp\left[-\frac{\hbar^2(\omega(\mathbf{q})_s - \omega)^2}{2\sigma^2}\right]}{\sum_{\mathbf{q}=0,s} \frac{1}{\Gamma(\mathbf{q})_s \sqrt{2\pi\sigma^2}} \exp\left[-\frac{\hbar^2(\omega(\mathbf{q})_s - \omega)^2}{2\sigma^2}\right]}, \quad (7)$$

$$\begin{aligned} \Gamma_2[\omega] &= p \cdot \omega^2, \\ p &= \frac{\sum_{\mathbf{q}=0,s} \int_{\omega_0}^{2\omega_0} d\omega_c \frac{\Gamma(\mathbf{q})_s}{\omega^2(\mathbf{q})_s \sqrt{2\pi\sigma^2}} \exp\left[-\frac{\hbar^2(\omega(\mathbf{q})_s - \omega_c)^2}{2\sigma^2}\right]}{\sum_{\mathbf{q}=0,s} \int_{\omega_0}^{2\omega_0} d\omega_c \frac{1}{\sqrt{2\pi\sigma^2}} \exp\left[-\frac{\hbar^2(\omega(\mathbf{q})_s - \omega_c)^2}{2\sigma^2}\right]}. \end{aligned} \quad (8)$$

Here, ω_0 is the smallest non-zero frequency when $\mathbf{q} = 0$, and $\sigma = 70 \text{ cm}^{-1}$ is a broadening parameter set large enough to ensure smooth averaging of linewidths. The full-order lattice anharmonicity is intrinsically considered for anharmonic linewidths extracted from the normal mode decomposition with ring-polymer or classical MD simulations (see Fig. S5 of SI for comparisons).

Voigt function A two-parameter distribution, denoted as $\mathcal{F}_{[\Gamma(\mathbf{q})_s + \Gamma(\mathbf{q})_{s'}, \eta]}$, is derived by convolving a Lorentzian with a full width at half maximum of $\Gamma(\mathbf{q})_s + \Gamma(\mathbf{q})_{s'}$ and a Gaussian with a variance of $\eta^2\pi/2$. This replaces the one-parameter distribution $\mathcal{F}_{[\Gamma(\mathbf{q})_s + \Gamma(\mathbf{q})_{s'}, \eta]}$ found in Eq. 4 within the WTE. Specifically, it involves a Gaussian distribution with a height of $\frac{1}{\pi\eta}$ (FWHM $\Delta_G = 2\sqrt{\pi \ln 2\eta}$) and a Lorentzian distribution with a height of $\frac{1}{\pi\gamma}$ (FWHM $\Delta_L = 2\gamma$). The convolution of these distributions is often expressed as the extended pseudo-Voigt function, employing an accurate and efficient numerical approximation. A detailed discussion can be found in refs. [29, 67]. The convergence test with respect to the broadening parameter η is shown in Fig. S8 of SI. In this work, η is equal to 5 cm^{-1} to compute rWTE κ .

WTE thermal conductivity of crystal $Cs_3Bi_2I_6Cl_3$ We obtained the temperature-dependent cubic and quartic interatomic force constants (IFCs) at 250 K and 300 K using the hiPhive package [68]. The harmonic terms at 0 K calculated using Phonopy [69] were subtracted from the atomic forces and only cubic and quartic IFCs were extracted to the residual force-displacement data. We collected the force-displacement data from RPMD simulations [70]. Three-phonon linewidths were calculated using the ShengBTE [71] package. Four-phonon linewidths were calculated using our code based on the formulae developed by Feng *et al.* [50, 51]. We carefully tested the relation between q -point mesh and κ , and a $6 \times 6 \times 6$ q -point mesh was used to compute the phonon linewidths and the κ of $Cs_3Bi_2I_6Cl_3$. The scatterbroad in the ShengBTE package, which determines the width of the Gaussian smearing function for numerically ensuring the energy conservation process in phonon-phonon scatterings, was set to 1 and 0.1 for the calculations of the three- and four-phonon scatterings, respectively. We also calculated the WTE conductivity based on our experimental lattice constants at 300 K, and the calculated WTE κ ($\kappa_x = 0.227 \text{ W m}^{-1} \text{ K}^{-1}$; $\kappa_z = 0.231 \text{ W m}^{-1} \text{ K}^{-1}$) based on experimental lattice constants show a better agreement with the measurements, compared to those based on the predicted lattice constants of NEP.

HNEMD and its quantum correction In HNEMD [47, 48], one applies an external driving force

$$\mathbf{F}_i^{\text{ext}} = \mathbf{F}_e \cdot \mathbf{W}_i \quad (9)$$

to generate a nonzero heat current. Here \mathbf{F}_e is the driving force parameter and \mathbf{W}_i is the virial tensor for atom i . Within the linear-response regime, the heat current \mathbf{J} is proportional to the driving force parameter as

$$\langle J^\alpha \rangle = TV \sum_\beta \kappa^{\alpha\beta} F_e^\beta, \quad (10)$$

where V is the volume of the simulated system, and α and β are Cartesian directions. Considering diagonal elements of the thermal conductivity tensor and dropping the tensor indices, the cumulative thermal conductivity in one direction can be

expressed as

$$\kappa(t) = \frac{1}{t} \int_0^t ds \frac{\langle J(s) \rangle}{TVF_e}. \quad (11)$$

The HNEMD approach [47] also allows for obtaining the spectral thermal conductivity

$$\kappa(\omega, T) = \frac{2}{VTF_e} \int_{-\infty}^{\infty} dt e^{i\omega t} K(t), \quad (12)$$

Here, $K(t)$ is the virial-velocity correlation function and its vectorial version is defined as

$$\mathbf{K}(t) = \sum_i \langle \mathbf{W}_i(0) \cdot \mathbf{v}_i(t) \rangle. \quad (13)$$

The classical spectral thermal conductivity $\kappa(\omega, T)$ can be quantum-corrected [49, 72] by multiplying it with the ratio of quantum-to-classical modal heat capacity:

$$\kappa^q(\omega, T) = \kappa(\omega, T) \frac{x^2 e^x}{(e^x - 1)^2}, \quad (14)$$

where $x = \hbar\omega/(k_B T)$.

Spectral Mean free path To compute the vibrational mean free paths (MFPs) of the vibrational modes, we first perform a single NEMD simulation in the ballistic limit (low T and short supercell length L), equivalent to the atomistic Green's function approach, and then employ the same spectral decomposition method as in HNEMD to obtain the spectral thermal conductance $G(\omega)$ [49]:

$$G(\omega) = \frac{2}{V\Delta T} \int_{-\infty}^{\infty} dt e^{i\omega t} K(t), \quad (15)$$

where ΔT is the temperature difference between the heat source and the heat sink in the NEMD setup. Then we can derive the spectral MFP as [47]

$$\lambda(\omega, T) = \kappa(\omega, T)/G(\omega). \quad (16)$$

Acknowledgments ZZ acknowledges the European Union's Horizon 2020 research and innovation programme under the Marie Skłodowska-Curie grant agreement No 101034413. The authors acknowledge the research computing facilities offered by HPC ISTA and ITS HKU.

[1] R. Peierls, "Zur kinetischen theorie der wärmeleitung in kristallen," *Annalen der Physik* **395**, 1055 (1929).

[2] Z. Zeng, X. Shen, R. Cheng, O. Perez, N. Ouyang, Z. Fan, P. Lemoine, B. Raveau, E. Guilmeau, and Y. Chen, "Pushing thermal conductivity to its lower limit in crystals with simple structures," *Nature Communications* **15**, 3007 (2024).

[3] W. Lee, H. Li, A. B. Wong, D. Zhang, M. Lai, Y. Yu, Q. Kong, E. Lin, J. J. Urban, J. C. Grossman, *et al.*, "Ultralow thermal conductivity in all-inorganic halide perovskites," *Proceedings of the National Academy of Sciences* **114**, 8693 (2017).

[4] B. Zink, R. Pietri, and F. Hellman, "Thermal conductivity and specific heat of thin-film amorphous silicon," *Physical review letters* **96**, 055902 (2006).

[5] D. G. Cahill, "Thermal conductivity measurement from 30 to 750 k: the 3ω method," *Review of scientific instruments* **61**, 802 (1990).

[6] P. W. Anderson, B. I. Halperin, and C. M. Varma, "Anomalous low-temperature thermal properties of glasses and spin glasses," *Philosophical Magazine* **25**, 1 (1972).

[7] W. Schirmacher, G. Ruocco, and T. Scopigno, "Acoustic atten-

uation in glasses and its relation with the boson peak," *Physical review letters* **98**, 025501 (2007).

[8] P. B. Allen and J. L. Feldman, "Thermal conductivity of glasses: Theory and application to amorphous si," *Physical review letters* **62**, 645 (1989).

[9] P. B. Allen and J. L. Feldman, "Thermal conductivity of disordered harmonic solids," *Physical Review B* **48**, 12581 (1993).

[10] P. Acharyya, T. Ghosh, K. Pal, K. S. Rana, M. Dutta, D. Swain, M. Etter, A. Soni, U. V. Waghmare, and K. Biswas, "Glassy thermal conductivity in cs3bi2i6cl3 single crystal," *Nature communications* **13**, 5053 (2022).

[11] B. Sun, S. Niu, R. P. Hermann, J. Moon, N. Shulumba, K. Page, B. Zhao, A. S. Thind, K. Mahalingam, J. Milam-Guerrero, *et al.*, "High frequency atomic tunneling yields ultralow and glass-like thermal conductivity in chalcogenide single crystals," *Nature Communications* **11**, 6039 (2020).

[12] B. Zhao, M. S. B. Hoque, G. Y. Jung, H. Mei, S. Singh, G. Ren, M. Milich, Q. Zhao, N. Wang, H. Chen, *et al.*, "Orientation-controlled anisotropy in single crystals of quasi-1d batis3," *Chemistry of Materials* **34**, 5680 (2022).

[13] M. S. B. Hoque, E. R. Hoglund, B. Zhao, D.-L. Bao, H. Zhou, S. Thakur, E. Osei-Agyemang, K. Hattar, E. A. Scott, M. Surendran, *et al.*, "Ruddlesden-popper chalcogenides push the limit of mechanical stiffness and glass-like thermal conductivity in crystals," *arXiv preprint arXiv:2312.02534* (2023).

[14] D. G. Cahill, S. K. Watson, and R. O. Pohl, "Lower limit to the thermal conductivity of disordered crystals," *Physical Review B* **46**, 6131 (1992).

[15] M. Beekman and D. G. Cahill, "Inorganic crystals with glass-like and ultralow thermal conductivities," *Crystal Research and Technology* **52**, 1700114 (2017).

[16] B. C. Sales, B. Chakoumakos, R. Jin, J. Thompson, and D. Mandrus, "Structural, magnetic, thermal, and transport properties of x 8 ga 16 ge 30 (x= e u, s r, ba) single crystals," *Physical Review B* **63**, 245113 (2001).

[17] M. Parrinello and A. Rahman, "Study of an F center in molten KCl," *The Journal of Chemical Physics* **80**, 860 (1984).

[18] R. P. Feynman, A. R. Hibbs, and D. F. Styer, *Quantum mechanics and path integrals* (Courier Corporation, 2010).

[19] J. Cao and G. A. Voth, "The formulation of quantum statistical mechanics based on the feynman path centroid density. iv. algorithms for centroid molecular dynamics," *The Journal of chemical physics* **101**, 6168 (1994).

[20] S. Habershon, D. E. Manolopoulos, T. E. Markland, and T. F. Miller III, "Ring-polymer molecular dynamics: Quantum effects in chemical dynamics from classical trajectories in an extended phase space," *Annual review of physical chemistry* **64**, 387 (2013).

[21] M. Rossi, M. Ceriotti, and D. E. Manolopoulos, "How to remove the spurious resonances from ring polymer molecular dynamics," *The Journal of chemical physics* **140** (2014).

[22] R. Luo and K. Yu, "Capturing the nuclear quantum effects in molecular dynamics for lattice thermal conductivity calculations: Using ice as example," *The Journal of Chemical Physics* **153** (2020).

[23] B. J. Sutherland, W. H. Moore, and D. E. Manolopoulos, "Nuclear quantum effects in thermal conductivity from centroid molecular dynamics," *The Journal of Chemical Physics* **154** (2021).

[24] G. Caldarelli, M. Simoncelli, N. Marzari, F. Mauri, and L. Benfatto, "Many-body green's function approach to lattice thermal transport," *Physical Review B* **106**, 024312 (2022).

[25] M. Simoncelli, N. Marzari, and F. Mauri, "Unified theory of thermal transport in crystals and glasses," *Nature Physics* **15**, 809 (2019).

[26] M. Simoncelli, N. Marzari, and F. Mauri, "Wigner formulation of thermal transport in solids," *Physical Review X* **12**, 041011 (2022).

[27] L. Isaeva, G. Barbalinardo, D. Donadio, and S. Baroni, "Modeling heat transport in crystals and glasses from a unified lattice-dynamical approach," *Nature communications* **10**, 3853 (2019).

[28] G. Barbalinardo, Z. Chen, N. W. Lundgren, and D. Donadio, "Efficient anharmonic lattice dynamics calculations of thermal transport in crystalline and disordered solids," *Journal of Applied Physics* **128** (2020).

[29] M. Simoncelli, F. Mauri, and N. Marzari, "Thermal conductivity of glasses: first-principles theory and applications," *npj Computational Materials* **9**, 106 (2023).

[30] A. Fiorentino, E. Drigo, S. Baroni, and P. Pegolo, "Unearthing the foundational role of anharmonicity in heat transport in glasses," *Physical Review B* **109**, 224202 (2024).

[31] Q. He and Y. Yang, "On lattice distortion in high entropy alloys," *Frontiers in Materials* **5**, 42 (2018).

[32] Z. Fan, Z. Zeng, C. Zhang, Y. Wang, K. Song, H. Dong, Y. Chen, and T. Ala-Nissila, "Neuroevolution machine learning potentials: Combining high accuracy and low cost in atomistic simulations and application to heat transport," *Physical Review B* **104**, 104309 (2021).

[33] Z. Fan, Y. Wang, P. Ying, K. Song, J. Wang, Y. Wang, Z. Zeng, K. Xu, E. Lindgren, J. M. Rahm, *et al.*, "Gpumd: A package for constructing accurate machine-learned potentials and performing highly efficient atomistic simulations," *The Journal of Chemical Physics* **157** (2022).

[34] J. P. Perdew, A. Ruzsinszky, G. I. Csonka, O. A. Vydrov, G. E. Scuseria, L. A. Constantin, X. Zhou, and K. Burke, "Restoring the density-gradient expansion for exchange in solids and surfaces," *Physical review letters* **100**, 136406 (2008).

[35] S. Grimme, S. Ehrlich, and L. Goerigk, "Effect of the damping function in dispersion corrected density functional theory," *Journal of computational chemistry* **32**, 1456 (2011).

[36] D. A. Keen and A. L. Goodwin, "The crystallography of correlated disorder," *Nature* **521**, 303 (2015).

[37] A. Simonov and A. L. Goodwin, "Designing disorder into crystalline materials," *Nature Reviews Chemistry* **4**, 657 (2020).

[38] X. Liang, J. Klarbring, W. J. Baldwin, Z. Li, G. Csányi, and A. Walsh, "Structural dynamics descriptors for metal halide perovskites," *The Journal of Physical Chemistry C* **127**, 19141 (2023).

[39] E. S. Božin, C. D. Malliakas, P. Souvatzis, T. Proffen, N. A. Spaldin, M. G. Kanatzidis, and S. J. Billinge, "Entropically stabilized local dipole formation in lead chalcogenides," *Science* **330**, 1660 (2010).

[40] E. G. Meekel and A. L. Goodwin, "Correlated disorder in metal-organic frameworks," *CrystEngComm* **23**, 2915 (2021).

[41] E. Fransson, M. Slabanja, P. Erhart, and G. Wahnström, "Dynisor—a tool for extracting dynamical structure factors and current correlation functions from molecular dynamics simulations," *Advanced Theory and Simulations* **4**, 2000240 (2021).

[42] O. Hellman, P. Steneteg, I. A. Abrikosov, and S. I. Simak, "Temperature dependent effective potential method for accurate free energy calculations of solids," *Physical Review B* **87**, 104111 (2013).

[43] T. Lanigan-Atkins, X. He, M. Krogstad, D. Pajerowski, D. Abernathy, G. N. Xu, Z. Xu, D.-Y. Chung, M. Kanatzidis, S. Rosenkranz, *et al.*, "Two-dimensional overdamped fluctuations of the soft perovskite lattice in cspbbr3," *Nature materials* **20**, 977 (2021).

[44] Y. Zhang, Y. J. Zhou, J. P. Lin, G. L. Chen, and P. K. Liaw,

“Solid-solution phase formation rules for multi-component alloys,” *Advanced engineering materials* **10**, 534 (2008).

[45] H. Song, F. Tian, Q.-M. Hu, L. Vitos, Y. Wang, J. Shen, and N. Chen, “Local lattice distortion in high-entropy alloys,” *Physical Review Materials* **1**, 023404 (2017).

[46] P. Acharyya, K. Pal, A. Ahad, D. Sarkar, K. S. Rana, M. Dutta, A. Soni, U. V. Waghmare, and K. Biswas, “Extended anti-bonding states and phonon localization induce ultralow thermal conductivity in low dimensional metal halide,” *Advanced Functional Materials* **33**, 2304607 (2023).

[47] Z. Fan, H. Dong, A. Harju, and T. Ala-Nissila, “Homogeneous nonequilibrium molecular dynamics method for heat transport and spectral decomposition with many-body potentials,” *Physical Review B* **99**, 064308 (2019).

[48] D. J. Evans, “Homogeneous nemd algorithm for thermal conductivity—application of non-canonical linear response theory,” *Physics Letters A* **91**, 457 (1982).

[49] Y. Wang, Z. Fan, P. Qian, M. A. Caro, and T. Ala-Nissila, “Quantum-corrected thickness-dependent thermal conductivity in amorphous silicon predicted by machine learning molecular dynamics simulations,” *Physical Review B* **107**, 054303 (2023).

[50] T. Feng and X. Ruan, “Quantum mechanical prediction of four-phonon scattering rates and reduced thermal conductivity of solids,” *Physical Review B* **93**, 045202 (2016).

[51] T. Feng, L. Lindsay, and X. Ruan, “Four-phonon scattering significantly reduces intrinsic thermal conductivity of solids,” *Physical Review B* **96**, 161201 (2017).

[52] J. Klarbring, O. Hellman, I. A. Abrikosov, and S. I. Simak, “Anharmonicity and ultralow thermal conductivity in lead-free halide double perovskites,” *Physical Review Letters* **125**, 045701 (2020).

[53] J. Li, L. Wei, Z. Ti, L. Ma, Y. Yan, G. Zhang, and P.-F. Liu, “Wavelike tunneling of phonons dominates glassy thermal conductivity in crystalline cs 3 bi 2 i 6 cl 3,” *Physical Review B* **108**, 224302 (2023).

[54] L. Lindsay, D. Broido, and T. Reinecke, “Phonon-isotope scattering and thermal conductivity in materials with a large isotope effect: A first-principles study,” *Physical review B* **88**, 144306 (2013).

[55] G. Kresse and J. Furthmüller, “Efficient iterative schemes for ab initio total-energy calculations using a plane-wave basis set,” *Physical review B* **54**, 11169 (1996).

[56] G. Kresse and D. Joubert, “From ultrasoft pseudopotentials to the projector augmented-wave method,” *Physical review b* **59**, 1758 (1999).

[57] P. Ying and Z. Fan, “Combining the d3 dispersion correction with the neuroevolution machine-learned potential,” *Journal of Physics: Condensed Matter* **36**, 125901 (2023).

[58] J. Wei, Z. Xia, Y. Xia, and J. He, “Hierarchy of exchange-correlation functionals in computing lattice thermal conductivities of rocksalt and zincblende semiconductors,” *arXiv preprint arXiv:2404.06346* (2024).

[59] Z. Fan, W. Chen, V. Vierimaa, and A. Harju, “Efficient molecular dynamics simulations with many-body potentials on graphics processing units,” *Computer Physics Communications* **218**, 10 (2017).

[60] M. Bernetti and G. Bussi, “Pressure control using stochastic cell rescaling,” *The Journal of Chemical Physics* **153** (2020).

[61] G. Bussi, D. Donadio, and M. Parrinello, “Canonical sampling through velocity rescaling,” *The Journal of chemical physics* **126** (2007).

[62] S. Thebaud, T. Berlijn, and L. Lindsay, “Perturbation theory and thermal transport in mass-disordered alloys: Insights from green’s function methods,” *Physical Review B* **105**, 134202 (2022).

[63] A. F. Harper, K. Iwanowski, W. C. Witt, M. C. Payne, and M. Simoncelli, “Vibrational and thermal properties of amorphous alumina from first principles,” *Physical Review Materials* **8**, 043601 (2024).

[64] A. Fiorentino, P. Pegolo, and S. Baroni, “Hydrodynamic finite-size scaling of the thermal conductivity in glasses,” *npj Computational Materials* **9**, 157 (2023).

[65] A. J. McGaughey and J. M. Larkin, “Predicting phonon properties from equilibrium molecular dynamics simulations,” *Annual review of heat transfer* **17** (2014).

[66] A. Carreras, A. Togo, and I. Tanaka, “Dynaphopy: A code for extracting phonon quasiparticles from molecular dynamics simulations,” *Computer Physics Communications* **221**, 221 (2017).

[67] T. Ida, M. Ando, and H. Toraya, “Extended pseudo-voigt function for approximating the voigt profile,” *Journal of Applied Crystallography* **33**, 1311 (2000).

[68] F. Eriksson, E. Fransson, and P. Erhart, “The hiphive package for the extraction of high-order force constants by machine learning,” *Advanced Theory and Simulations* **2**, 1800184 (2019).

[69] A. Togo and I. Tanaka, “First principles phonon calculations in materials science,” *Scripta Materialia* **108**, 1 (2015).

[70] Z. Li, Y. Xia, and C. Wolverton, “First-principles calculations of lattice thermal conductivity in tl 3 vse 4: Uncertainties from different approaches of force constants,” *Physical Review B* **108**, 184307 (2023).

[71] W. Li, J. Carrete, N. A. Katcho, and N. Mingo, “Shengbte: A solver of the boltzmann transport equation for phonons,” *Computer Physics Communications* **185**, 1747 (2014).

[72] J. Turney, A. McGaughey, and C. Amon, “Assessing the applicability of quantum corrections to classical thermal conductivity predictions,” *Physical Review B* **79**, 224305 (2009).